RSC Advances

This is an *Accepted Manuscript*, which has been through the Royal Society of Chemistry peer review process and has been accepted for publication.

Accepted Manuscripts are published online shortly after acceptance, before technical editing, formatting and proof reading. Using this free service, authors can make their results available to the community, in citable form, before we publish the edited article. This *Accepted Manuscript* will be replaced by the edited, formatted and paginated article as soon as this is available.

You can find more information about *Accepted Manuscripts* in the **Information for Authors**.

An air-assisted activation strategy for porous carbon spheres and its enhanced electrochemical performance

Huaqing Xuan,[a] Yiliang Wang,[a] Gaoxing Lin,[a] Fan Wang,[a] Lin Zhou,[a] Xiaoping Dong[a*] and Zhi Chen[b*]

[a] Department of Chemistry, School of Sciences, Zhejiang Sci-Tech University, 928 Second Avenue, Xiasha Higher Education Zone, Hangzhou, China.

Fax: +86 571 86843228; Tel: +86 571 86843228; E-mail: xpdong@zstu.edu.cn

[b] College of Materials Science and Engineering, China Jiliang University, 258 Xueyuan Street, Xiasha Higher Education Zone, Hangzhou310018, China.

Fax: +86 571 86835738; Tel: 189 690 29559; E-mail: zchen@gmail.com

Abstract

Activated porous carbons are of increasing interests in supercapacitors due to the superior porosity and facile preparation. However, their porous structure is strongly dependent on activation procedures. Herein, we reported an air-assisted approach to activate spherical resorcinol-formaldehyde resin to obtain porous carbons, which avoided the use of inert atmosphere and additionally chemical activating agent. The porous structures of obtained activated carbon spheres (AACS) were related to the activation time, and the percentage of mesopores gradually increased as prolonging time to 6 h. The 6 h activated sample AACS-6 achieved a largest pore volume (1.01 cm g^{-1}) and a highest BET surface area (2178 m^2 g^{-1}). The optimal electrochemical performance was realized on AACS-6 that exhibited a large specific capacitance of 222 F g^{-1} at 0.5 A g^{-1} in a three-electrode system. Slightly decrease of capacitance (12.5%) was obtained as increase the current density to 20 A g^{-1}, indicating the significant rate capability. Furthermore, AACS-6 showed excellent cycling stability that a ~97% retention of initial capacitance was obtained after 5000 cycles. The assembled AACS-6 based symmetric cell achieved a

1

high energy density of 10.1 Wh kg^{-1} at a power density of 398.7 W kg^{-1} in the potential range of 0~1.6

V in 0.5 M Na_2SO_4 aqueous electrolyte.

Introduction

Energy consumption relying on the depletion of non-renewable fossil fuels leads to energy crisis and

aggravating environmental pollution. Currently, environment protection and energy supply have

became two of the most important topics.[1,2] Electrochemical capacitors (also called ultracapacitors or

supercapacitors) are selected because of a wide range of applications and numerous superiorities, such

as excellent charge-discharge performance, high energy and power density, uninterruptable power

sources and environment friendliness compared with traditional batteries.[3,4] Electrochemical capacitors

are divided into electrical double-layer capacitors (EDLCs) and pseudocapacitors according to different

energy storage mechanism. Possessing high energy density in comparison with EDLCs, however,

pseudocapacitors are poor in cycle stability and power density. Contrarily, EDLCs exhibit long cycle

life and rapid charge-discharge rate, whereas the relatively low capacitance value limits their practical

applications. Therefore, it is vital to develop advanced electrode materials with high capacitance for

EDLCs.[5,6]

From the viewpoint of energy storage mechanism, rapid electron transfer and large surface area for

accumulation of electrolyte ions are required for the electrode materials of high performance EDLCs.

Porous carbonaceous materials are undoubtedly the optimum candidate for EDLCs due to their high

electron conductivity, large surface area and developed porosity for electrolyte diffusion. Up to date,

numerous porous carbons have attracted tremendous attentions, such as activated carbons (ACs),

ordered mesoporous carbons, carbon aerogels, carbon nanotubes (CNTs) and graphene based materials.

[7-10] Among them, ACs are most widely adopted in practical application because of its easily-formed

micropores, large surface area, good conductivity, low cost and industrialization production. It is worth

mentioning that large specific surface area and abundant active sites of commercial ACs are usually

contributed by micropores. When at a high current density, micropores are always hard to be accessible

by electrolyte ions. It has been proved that mesopores are committed to accelerate the ion migration to

obtain higher specific capacitance compared with micropores.[11] A good match for the pore size and the

dimension of electrolyte ions is necessary for high specific capacitance.[12-14] It is confirmed that carbon

material with mesopores (2-5 nm) are superior in increasing the energy density and power density.[15] So

designing ACs with pores large enough to be accessible to electrolyte and small enough to achieve a

large surface area is necessary.[16]

Two main methods are usually employed to prepare ACs: physical activation and chemical

activation. The agents of the physical activation are steam, O_2 or CO_2, whereas KOH, $ZnCl_2$ and H_3PO_4

are used in chemical activation.[17-21] Lv et al. reported the mesoporous carbons from FDU-15 via KOH

activation with a specific capacitance of 200 F g^{-1} at a current density of 1 A g^{-1} in 6 M KOH.[22] Wang et

al. synthesized the mesoporous resorcinol-formaldehyde resin carbons by the means of $ZnCl_2$

activation acquiring a specific capacitance of 204 F g^{-1} in 2 M KOH at a current density of 0.5 A g^{-1}.[23]

Chen et al. used H_3PO_4 to activate cotton stalk and obtained microporous carbons with a specific

capacitance of 114 F g^{-1} in 1 M Et_4NBF_4 electrolytes at 0.5 A g^{-1}.[24] Wu et al. activated firewoods via

steam activation reached 120 F g^{-1} in acidic electrolytes at 200 mV s^{-1}.[25] However, chemical activation

is time-consuming and environment-polluting. Additionally, it must be carried out in an inert

atmosphere. And traditional physical activation is always divided into two steps: carbonization and

activation.

In this work, we reported a facile and activation agent-free method to synthesize porous carbons by

an air-assisted activation using resorcinol-formaldehyde (RF) as precursor. The one-step

carbonization/activation process and the avoiding of inert atmosphere and agents made this activation

strategy much more time-saving and economical. The obtained air-activated carbon spheres (AACSs)

presented a large surface area and good rate capability in a three-electrode system. Furthermore, the

symmetric supercapacitor assembled by AACS-6 also achieves excellent electrochemical performance.

Experimental

All the chemical regents in this work were of analytical grade purity and used without further

purification.

Synthesis of resorcinol-formaldehyde resin spheres

Resorcinol-formaldehyde resin spheres were synthesized via the stöber method using the resorcinol

and formaldehyde solution as previously reported.[26] Firstly, 2.5 mL ammonia aqueous solution

(NH_4OH, 25 wt%) was added into the mixture of 500 mL deionized water and 200 mL absolute ethanol.

After stirring for 1 h, 5 g resorcinol was added to this ammonia solution, followed by a continuous

stirring for 30 min. Subsequently, 7 mL formaldehyde (HCHO, 37 wt%) was added into the solution

and stirred at 30 $^{\circ}$C for 24 h. The resultant solution was transferred into a Teflon-sealed autoclave and

heated at 100 $^{\circ}$C for 24 h. The products were obtained by suction filtration and air-dried for 10 h.

Synthesis of AACSs

Typically, 3g brownish resorcinol-formaldehyde resins were placed in a corundum crucible with

cover and directly transferred into the muffle furnace with high temperature of 900 $^{\circ}$C by crucible tongs,

then calcined for several hours. The prepared products were denoted as AACS-X (X= 1, 2, 3, 4, 5 and 6

h, referring to the activation time).

Characterizations

X-ray diffraction (XRD) patterns were estimated by a DX-2700 diffractometer (Dandong Haoyuan

Instrument Co. Ltd., China) using Cu Kα radiation (λ = 0.15418 nm) as an X-ray source. Nitrogen

adsorption-desorption isotherm measurements were performed at -196 $^{\circ}$C with a micromeritics ASAP

2020 surface area analyzer. The samples were out-gassed at 150 $^{\circ}$C for 6 h. The specific surface area

(S_{BET}) was tested using the Brunauer-Emmett-Teller (BET) method. The pore size distributions were

estimated according to density functional theory (DFT) method. The total pore volume was calculated

according to single point method at relative pressure (P/P_0) = 0.975. The morphology of the products

was observed by scanning electron microscope (SEM, Hitachi S-4800) and JEOL JEM-2100

transmission electron microscope (TEM) with an accelerating voltage of 200 kV. Raman spectra of the

samples were measured using a Renishaw inVia Raman microscope (NCNST, China) at an excitation

wavelength of 514 nm.

Electrochemical measurements

The electrochemical properties were estimated via a three electrode system in 6 M KOH aqueous

solution on a CHI660D electrochemical station (Chenhua, Shanghai, China). A platinum foil and an

Ag/AgCl electrode were used as counter and reference electrodes, respectively. The working electrodes

were fabricated by mixing active material, carbon black and polyvinylidene fluoride (PVDF) with a

weight ratio of 7.5:1.5:1. Then the slurry-like product was coated onto Ni foam (1 cm×1 cm) and dried

at 100 $^{\circ}$C before being pressed under a pressure of 20 MPa. Cyclic voltammetry (CV) was performed

in the potential range from -1.1 V to -0.1 V at different scan rates of 10~500 mV s^{-1}. Galvanostatically

charge/discharge examinations were measured at different current densities of 0.5~20 A g^{-1}. The

symmetric supercapacitor consists of two working electrodes with a cellulose acetate membrane as

separator in the two-electrode system. Electrochemical impedance spectroscopy (EIS) was estimated in

open circuit voltage with an AC amplitude of 5 mV in a frequency range from 0.01 Hz to 100 kHz.

Results and discussion

Structural properties of AACSs

The possible mechanism of air-assisted activation for preparation of AACSs is shown in Scheme 1. It has been testified that the pyrolysis of resorcinol-formaldehyde resin spheres under high temperature would introduce microporous structure after releasing quantities of small molecules.[27] In the meantime, the resorcinol-formaldehyde resin spheres were converted to carbon spheres and the sphere diameter reduced because of the structural shrinkage. With the air assistance, some carbons in the spheres were burnt by O_2 in air, which would produce much more pores and enlarge the pore size. It is obvious that the porous structure of AACSs is dependent on the activation time. In consideration of the AACSs yield (as listed in Table 1), we controlled the activation time in six hours. It should be mentioned that the ~10% yield under 6 h activation in air is comparable with that using KOH activation, one of the most used chemical activation agent in ACs preparation.

Electronic microscopy technologies were employed to demonstrate the morphological and structural properties of AACSs materials (Fig. 1). As presented in Fig. 1a, the monodisperse spherical resorcinol-formaldehyde resin has a diameter of 800~900 nm. With carbonizing resorcinol-formaldehyde spheres in air for 6 hours, the spherical aspect is well maintained (Fig. 1b). However, the sphere size is apparently minified because of structural shrinkage and the diameter of AACS-6 is estimated as ~500 nm. The TEM images of AACS-6 are depicted in Fig. 1c and d. The uniform spherical morphology of AACS-6 can be seen obviously that is in accordance with SEM observation. It can also be observed that a large number of nanopores are distributed over the surface of AACS-6 due to the air activation.

6

Fig. 2a exhibits the XRD patterns of three samples with different activation time in air. All of the samples present two typically broad peaks of amorphous carbonaceous materials at 20~30° and 40~50°, which can be respectively ascribed to the graphitic (002) and (100) diffractions. It is noteworthy that the intensity of peaks gradually weakens from AACS-1 to AACS-6 in XRD pattern. This is related to the gradual diminish of graphite micro-crystallite zones in AACSs as prolonging the activation time in air. Fig. 2b shows Raman spectra of the samples. Two apparent peaks in the spectra are observed for each sample at 1350 cm^{-1} and 1590 cm^{-1}, respectively, corresponding to the D band and G band, representing disordered carbon and graphitic carbon.[28,29] It is estimated from Raman spectra that the I_D/I_G ratio of the samples from AACS-1 to AACS-6 is 1.64, 1.91, 1.92, 1.93, 1.95, 1.97, respectively, indicating the increased structural defects caused by prolonging the activation time for our amorphous carbons.[39-41]

Nitrogen sorption technology was used to describe the porous structure of AACSs materials. The carbon spheres (CS) material by carbonizing resorcinol-formaldehyde spheres under nitrogen atmosphere exhibits a type I isotherm (Fig. S1). It belongs to typical microporous structure that is illustrated by its pore size distribution. Nitrogen adsorption-desorption isotherms and corresponding pore size distribution curves of AACSs are exhibited in Fig. 3. As presented in Fig. 3a, although these isotherms of AACSs are still attributed to type I curve, the leap of absorbed N_2 volume is step by step expanded to high pressure region with the increase of activation time, which indicates the enhancement of mesopore percentage in the whole porosity of AACSs. This conclusion is demonstrated by the pore size distribution in Fig. 3b. In addition, the adsorbed N_2 volume improves in the same trend, suggesting the increase of surface area and pore volume. Their pore structure parameters are listed in Table 1. With the absence of air atmosphere, the CS sample displays a 1420 m^2 g^{-1} BET specific surface area that is

mainly contributed by microporous surface area (1110 m^2 g^{-1}). With prolonging the activation time

from 1 to 4 h, the S_{micro} value firstly gradually increases and then slowly decreases as the reaction time

from 4 to 6 h. On the contrary, the S_{meso} value continuously increases upon the prolonging of activation

time. These results suggest the formation process of porous structure: (1) The high-temperature

pyrolysis of polymers produces abundant micropores; (2) under air activation, micropores are further

developed and (3) the produced micropores are enlarged to mesopores by combination of partial carbon

framework in AACSs. The optimal sample AACS-6 possesses a largest BET specific surface area of

2178 m^2 g^{-1}, a highest mesopore percentage and a biggest pore volume of 1.01 cm^3 g^{-1}. Such superior

porous structure of AACSs implies that these materials have promising potentials in electrochemical

applications.

Electrochemical Performance of AACSs

The electrochemical properties of AACSs samples were investigated in 6 M KOH aqueous solution

by a three-electrode system. As shown in Fig. 4a, cyclic voltammetry (CV) profiles of AACSs depict

similar quasi-rectangular shapes at 50 mV s^{-1} in the potential from -1.1 V to -0.1 V, indicating that the

energy is stored by forming electrochemical double-layer.[11] The enclosed area by CV curve increases

upon the enhancement of activation time, and the AACS-6 electrode shows a biggest area that suggests

a highest specific capacitance. The specific capacitance of AACSs at different scan rates calculated

based on CV curves is as following equation:[30]

$$C = \frac{\int I dV}{mVv} \qquad (1)$$

where I (A) is the corresponding current, m (g) is the mass of electroactive material in the electrode, V

(V) is the potential, v (mV s^{-1}) is the scan rate. The detailed specific capacitances of AACSs are listed

in Table S1. At the scan rate of 50 mV s^{-1}, the specific capacitance of AACS-6 electrode is calculated to

be 214 F g^{-1}, which is much larger than that of the CS sample (115.9 F g^{-1} calculated from the CV curve

in Fig. S2a) and those of other AACSs samples.

Fig. 4b illustrates the galvanostatic charge/discharge (GCD) curves of AACSs at the current density

of 1 A g^{-1}. The curves are highly linear and symmetrical, meaning that the AACSs electrode materials

have excellent electrochemical reversibility. The specific capacitances of electrodes are calculated by

the following equation:[30]

$$C = \frac{I\Delta t}{m\Delta V} \qquad (2)$$

where Δt (s) is discharge time and ΔV (V) is the potential range. The CS electrode shows a much

shorter discharging time and low specific capacitance of 118 F g^{-1} (Fig. S2b). The enhancement of

calculated specific capacitance of AACSs follows the similar sequence in CV results (detailed values

shown in Table S1). The highest specific capacitance of 212 F g^{-1} is obtained by the AACS-6 electrode,

which is consistent with the value in CV curve.

The electrochemical performance of the optimal electrode AACS-6 was further investigated. Fig. 5a

displays the CV curves of AACS-6 at different scan rates. The curves show distortion with the

increment of scan rate due to the internal resistance (IR) increase of electrode and electrolyte.[31]

However, even at a high scan rate of 500 mV s^{-1}, the CV profile still remains quasi-rectangular. This

can be attributed to the well-developed pore structure and high conductivity of AACS-6. The specific

capacitance of the AACS-6 electrode are 223, 206, 196, 183, 174, 165 and 157 F g^{-1} at scan rates from

10 to 500 mV s^{-1}, respectively. High capacitance retention up to 70% at 500 mV s^{-1} compared to that of

10 mV s^{-1} is acquired, which implies the significantly high rate capability of AACS-6 electrode and

shows promising potential for the applications needed high-power output. Fig. 5b illustrates the GCD

curves of AACS-6 under different current densities from 0.5 to 20 A g^{-1}. All the curves display relative

symmetric triangular shapes, which is another characteristic of an ideal EDLC. The detailed specific

capacitances at various current densities are plotted in Fig. 5c. A slight decrease of specific capacitance

with the current density increasing indicates that the electrode allows rapid ion diffusion and presents

excellent electrochemical utilization. The specific capacitance of AACS-6 is 222 F g^{-1} at 0.5 A g^{-1},

which is higher than those of other porous carbons synthesized by different activation methods (Table

S2). About 87.5% specific capacitance is retained as increasing the current density to a very high value

of 20 A g^{-1}. This remarkable capacitive performance should be contributed by the high surface area and

excellent pore structure. And, such splendid rate capability is even better than those of porous

carbonaceous materials in crystalline graphite structure.[32] The long-cycling stability of AACS-6

material was investigated by means of GCD cycling techniques at the current density of 5 A g^{-1} (Fig.

5d). The standout durability and recyclability are demonstrated by the above 99% initial capacitance

retention after 5000 cycles. The inset in Fig. 5d is the comparison of GCD curves of the 1st and the

5000th cycle, where the similar triangular shape and discharge time are observed. Moreover, no

difference of voltage drop between these two curves suggests that the internal resistance for AACS-6

electrode did not obviously increase after 5000 cycles.

The electrochemical performance of AACS-6 was further measured in 0.5 M Na$_2$SO$_4$ aqueous

solution with a two-electrode system. The CV curves of symmetric cell were shown in Fig. 6a at the

scan rate of 20 mV s^{-1} under different potential windows, which still remain nearly rectangular shape

under a potential window of 0~1.6 V. CV profile at different scan rate from 50 mV s^{-1} to 500 mV s^{-1} can

be observed in Fig. 6b, which still retains quasi-rectangular even at a high scan rate of 500 mV s^{-1},

indicating the high rate capability of the symmetric supercapacitor. Fig. 6c illustrates the GCD curves

of AACS-6 under different current densities from 0.5 A g^{-1} to 20 A g^{-1}. The voltage drop at the initiation

10

of the discharge is 0.001 V for the current density of 1 A g^{-1}, proving an extremely low IR of AACS-6.

The specific capacitances of the sample at different scan rates from 50 mV s^{-1} to 500 mV s^{-1} are plotted

in Fig. 6d and of which is 125.6 F g^{-1} at 50 mV s^{-1}. About 80.3% specific capacitance is retained as

increasing the scan rate to 500 mV s^{-1}.

Fig.7a is the Ragone plot of the symmetric cell obtained from the GCD curves. The spectific power

density (P, W kg^{-1}) and energy density (E, Wh kg^{-1}) of the electrodes are calculated by the following

equations:[33,34]

$$E = \frac{1}{2}CV^2 \qquad (3)$$

$$P = \frac{E}{t} \qquad (4)$$

Where C is the spectific capacitance of the symmetric cell, V is the potential range after IR drop in

GCD curve and t is the discharge time. The energy density of the cell is 10.1 Wh kg^{-1} at a power density

of 398.7 W kg^{-1} and still retains 8.7 Wh kg^{-1} at a power density of 8000.1 W kg^{-1}, which well meets the

demands for industrial application.

Electrochemical impedance spectroscopy (EIS) was applied to further study the electrochemical

behaviors of the symmetric cell (Fig. 7b). As illustrated in Nyquist plot, the steep line with high slope

in low frequency region indicates the nearly ideal capacitive behavior. The intercept is defined as

solution resistance (R_s). The small semicircle in high-frequency region corresponds to the interfacial

charge-transfer process and the diameter of semicircle is described as the charge-transfer resistance

(R_{ct}).[35,36] The inset is the fitted equivalent compromising five parts: R_s, R_{ct}, W (the Warburg

impendance), C_{dl} (the double layer capacitance), CPE (the constant phase element). It could be

evaluated from EIS data that the R_s and R_{ct} values are 0.98 Ω and 0.35 Ω, respectively, implying a low

internal resistance of the symmetric supercapacitor.

Conclusions

In conclusion, an air-activated porous carbon derived from resorcinol-formaldehyde resin with micro/mesoporous structure was produced by one-step carbonization/activation. The superb porosity of AACS-6 was achieved with high BET surface area (2178 $m^2 g^{-1}$) and the pore volume (1.01 $cm^3 g^{-1}$), of which is mainly contributed from mesopores. Thanks to the outstanding pore structure, the AACS-6 electrode shows excellent electrochemical performance, such as high specific capacitance, low internal resistance, perfect cycling stability, etc. Especially, the extremely high rate capability suggests its promising application in devices where a high power density is needed. What is more, this convenient air-assisted activation strategy provides a general approach to obtain the porous carbonaceous materials in various morphologies and microstructures for a variety of applications. Besides, the assembled symmetric supercapacitor also exhibits excellent energy density and power density in neutral electrolyte.

Acknowledgement

Notes and references

1   B. You, J. Jiang, S. Fan, *ACS Appl. Mater. Interfaces*, 2014, **6**, 15302.

2   H. Park, J. Seo, M. Kim, S. H Baeck, S. E. Shim, *Synthetic Metals*, 2015, **199**, 121.

3   J. Xu, Q. Gao, Y. Zhang, Y. Tan, W. Tian, L. Zhu, L. Jiang, *Sci. Rep.*, 2014, **4**, 5545.

4   V. Subramanian, C. Luo, A. M. Stephan, K. S. Nahm, S. Thomas, B. Wei, *J. Phys. Chem. C*, 2007, **111**, 7527.

5   L. Zhang, X. Zhao, *Chem. Soc. Rev.*, 2009, **38**, 2520.

6   C. Liu, Z. Yu, D. Neff, A. Zhamu, B. Jang, *Nano Lett.*, 2010, **10**, 4863.

7   A. Burke, *Electrochim. Acta*, 2007, **53**, 1083.

8   W. Xing, S. Qiao, R. Ding, F. Li, G. Lu, Z. Yan, H. Cheng, *Carbon*, 2006, **44**, 216.

9   R. W. Pekala, J. C. Farmer, C. T. Alviso, T. D. Tran, S. T. Mayer, J. M. Miller, B. Dunn, *J. Non-Cryst. Solids*, 1998, **225**, 74.

10 D. N. Futaba, K. Hata, T. Yamada, T. Hiraoka, Y. Hayamizu, Y. Kakudate, O. Tanaike, H. Hatori, M. Yumura, S. Iijima, *Nat. Mater.*, 2006, **5**, 987.

11 A. G. Pandolfo, A. F. Hollenkamp, *J. Power Sources*, 2006, **157**, 11.

12 B. Xu, F. Wu, R. Chen, G. Cao, S. Chen, Y. Yang, *J. Power Sources*, 2010, **195**, 2118.

13 C. O. Ania, J. Pernak, F. Stefaniak, E. Raymundo-Pinéro, F. Béguin, *Carbon*, 2006, **44**, 3113.

14 H. Liu, G. Zhu, *J. Power Sources*, 2007, **171**, 1054.

15 P. Simon, Y. Gogotsi, *Nat. Mater.*, 2008, **7**, 845.

16 J. Chmola, G. Yushin, R. K. Dash, Y. Gogotsi, J. E. Fischer, *Adv. Funct. Mater.*, 2006, **16**, 2288.

17 X. Xiang, E. Liu, Z. Huang, H. Shen, Y. Tian, C. Xiao, J. Yang, Z. Mao, *J. Solid State Electrochem.*, 2011, **15**, 2667.

18 K. Xia, Q. Gao, J. Jiang, J. Hu, *Carbon*, 2008, **46**, 1718.

19 M. Valix, W. Cheung, K. Zhang, *Adsorption*, 2008, **14**, 711.

20 X. He, R. Li, J. Han, M. Yu, M. Wu, *Mater. Lett.*, 2013, **94**, 158.

21 T. E. Rufford, D. Hulicova-Jurcakova, K. Khosla, Z. Zhu, G. Lu, *J. Power Sources*, 2010, **195**, 912.

22 Y. Lv, F. Zhang, Y. Dou, Y. Zhai, J. Wang, H. Liu, Y. Xia, B. Tu, D. Zhao, *J. Mater. Chem.*, 2012, **22**, 93.

23 Y. Wang, B. Chang, D. Guan, X. Dong, *J. Solid State Electrochem.*, 2015, **19**, 1783.

24 M. Chen, X. Kang, T. Wumaier, J. Dou, B. Gao, Y. Han, G. Xu, Z. Liu, L. Zhang, *J. Solid State Electrochem.*, 2013, **17**, 1005.

25 F. Wu, R. Tseng, C. Hu, C. Wang, *J. Power Sources*, 2004, **138**, 351.

26 J. Liu, S. Qiao, H. Liu, J. Chen, A. Orpe, D. Zhao, G. Lu, *Angew. Chem. Int. Ed.*, 2011, **50**, 5947.

27 V. G. Pol, L. K. Shrestha, K. Ariga, *ACS Appl. Mater. Interfaces*, 2014, **6**, 10649.

28 G. Wang, J. Yang, J. Park, X. Gou, B. Wang, H. Liu, J. Yao, *J. Phys. Chem. C*, 2008, **112**, 8192.

29 K. Krishnamoorthy, G. S. Kim, S. J. Kim, *Ultrason. Sonochem.*, 2013, **20**, 644.

30 E. Jokar, A. I. Zad, S. Shahrokhian, *J. Solid State Electrochem.*, 2015, **9**, 1269.

31 J. Zhang, J. Lee, *ACS Sustain Chem. Eng.*, 2014, **2**, 735.

32 B. Chang, Y. Guo, Y. Li, H. Yin, S. Zhang, B. Yang, X. Dong, *J. Mater. Chem. A*, 2015, **3**, 9565.

33 M. Li, J. Xue, *J. Phys. Chem. C*, 2014, **118**, 2507.

34 Q. Wang, J. Yan, Y. Wang, T. Wei, M. Zhang, X. Jing, Z. Fan, *Carbon*, 2014, **67**, 119.

35 Q. Qu, B. Wang, L. Yang, Y. Shi, S. Tian, Y. Wu, *Eletrochem, Commun.*, 2008, **10**, 1652.

36 Y. Zhu, S. Murali, M. D. Stoller, K. J. Ganesh, W. Cai, P. J. Ferreira, A. Pirkle, R. M. Wallace, K. A. Cychosz, M. Thommes, D. Su, E. A. Stach, R. S. Ruoff, *Science*, 2011, **332**, 1537.

37 Z. Li, W. Lv, C. Zhang, B. Li, F. Kang, Q. Yang, *Carbon*, 2015, **92**, 11.

38 B. Chang, Y. Wang, K. Pei, S. Yang, X. Dong, *RSC Adv.*, 2014, **4**, 40546.

39 G. Ma, D. Guo, K. Sun, H. Peng, Q. Yang, X. Zhou, *RSC Adv.*, 2015, **5**, 64704.

40 G. Ma, Q. Yang, K. Sun, H. Peng, F. Ran, X. Zhao, Z. Lei, *Bioresource Technology*, 2015, **197**, 137.

41 L. Zhu, Q. Gao, Y. Tan, W. Tian, J. Xu, K. Yang, C. Yang, *Microporous and Mesoporous Materials*,

2015, **210**, 1.
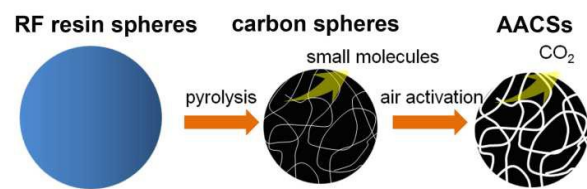
Scheme 1 The possible mechanism for formation of AACSs by an air-assisted activation strategy.

Table 1 The comparison of pore parameters and yields of AACSs and CS

Sample	S_{BET} [a] $(m^2\,g^{-1})$	S_{micro} [b] $(m^2\,g^{-1})$	S_{meso} [c] $(m^2\,g^{-1})$	V_{micro} [d] $(cm^3\,g^{-1})$	V_t [e] $(cm^3\,g^{-1})$	D [f] (nm)	Y [g] (wt%)
AACS-1	951.7	822.7	129.0	0.38	0.46	1.48/2.34	36.8
AACS-2	1379.4	1062.1	317.3	0.49	0.69	1.48/2.00	24.2
AACS-3	1636.2	1218.1	355.1	0.58	0.74	1.48/2.00	22.6
AACS-4	1748.2	1286.6	461.6	0.58	0.83	1.59/2.00	21.5
AACS-5	2006.9	1104.7	902.2	0.49	0.92	1.36/2.16	14.9
AACS-6	2178.2	1004.5	1173.7	0.43	1.01	1.59/2.00	10.5
CS	1420.2	1110.6	309.6	0.48	0.69	1.48/2.00	30.5

[a] BET specific surface area.

[b] Micropore surface area calculated with the *V-t* plot method.

[c] Mesopore surface area calculated with the *V-t* plot method.

[d] Micropore volumes calculated with the *V-t* plot method.

[e] The total pore volumes calculated by single adsorption at P/P_0=0.975.

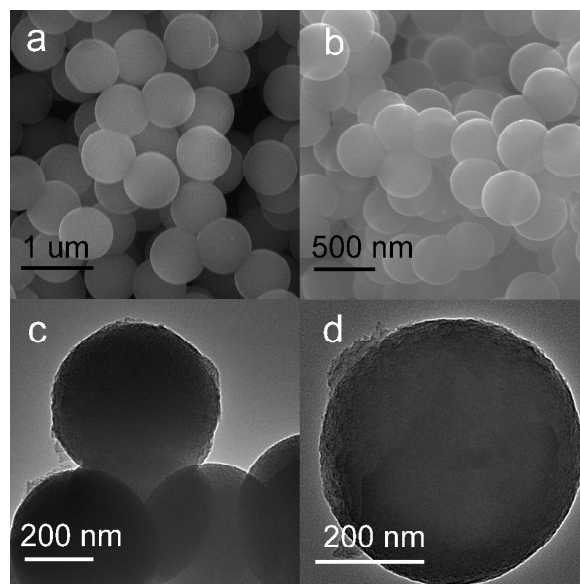[f] Pore size calculated with DFT method.

[g] Yields.

Fig. 1 SEM images of resorcinol-formaldehyde resin (a) and AACS-6 (b). TEM images of AACS-6 (c, d).
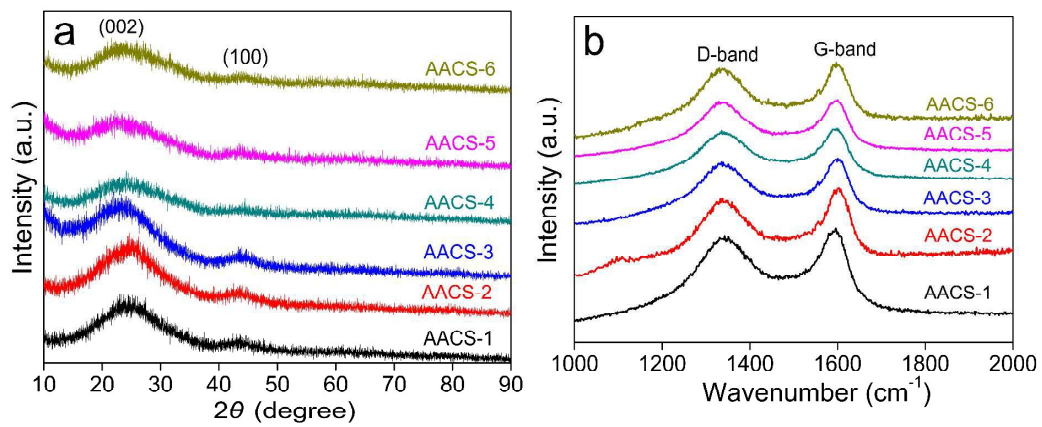
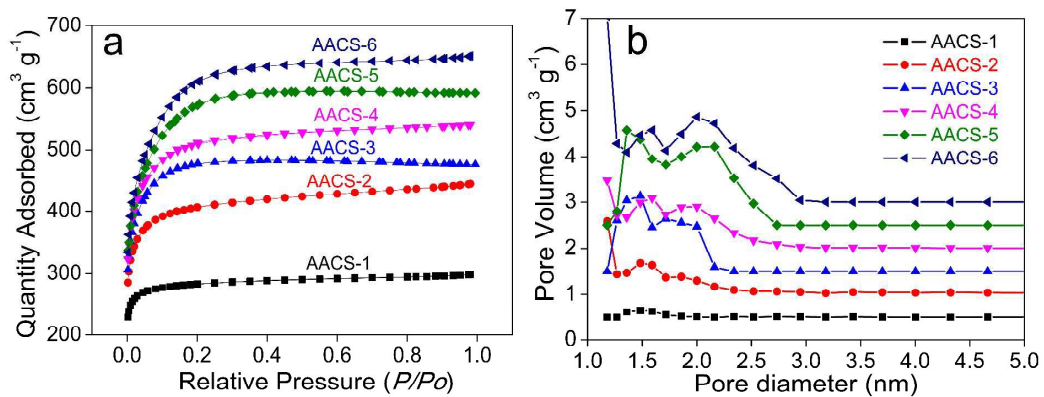**Fig. 2** XRD patterns (a) and Raman spectra (b) of AACSs

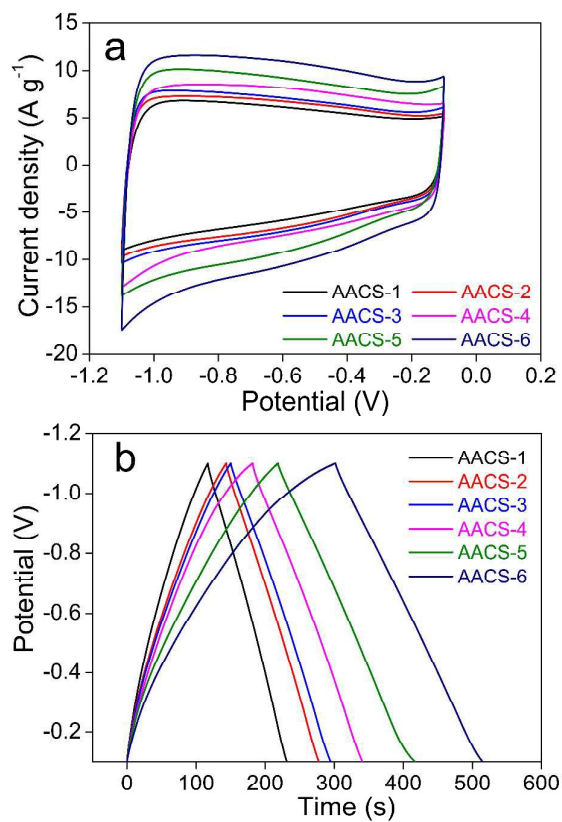**Fig. 3** N_2 adsorption-desorption isotherms (a) and the pore size distribution curves (b) of AACSs.

Fig. 4 Electrochemical capacitive behaviors of the AACSs samples. (a) CV measurements of AACSs at the scan rate of 50 mV s^{-1}. (b) Galvanostatic charge-discharge profiles of AACSs at the current density of 1 A g^{-1}.
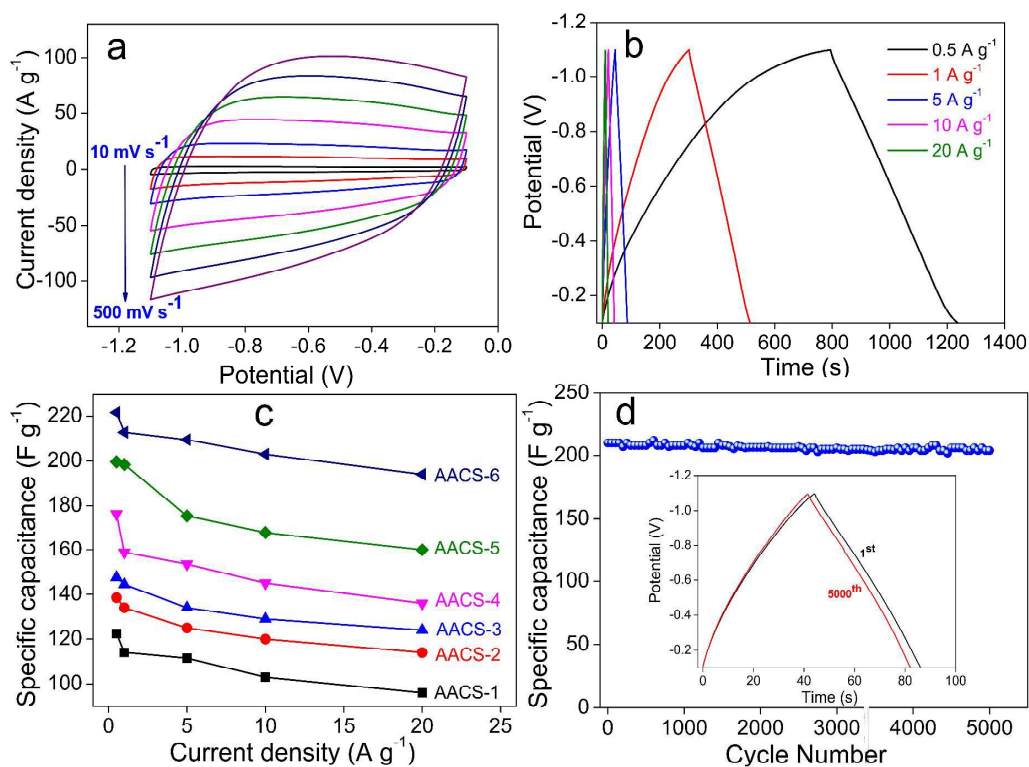
Fig. 5 Electrochemical capacitive behaviors of the AACS-6 sample. (a) CV measurements at different

scan rates in 6 M KOH aqueous electrolyte system. (b) Galvanostatic charge-discharge profiles at

different currents in 6 M KOH aqueous electrolyte system. (c) Specific capacitance of AACSs measured

at different currents. (d) The long-cycling stability of AACS-6 material at the current density of 5 A g^{-1}

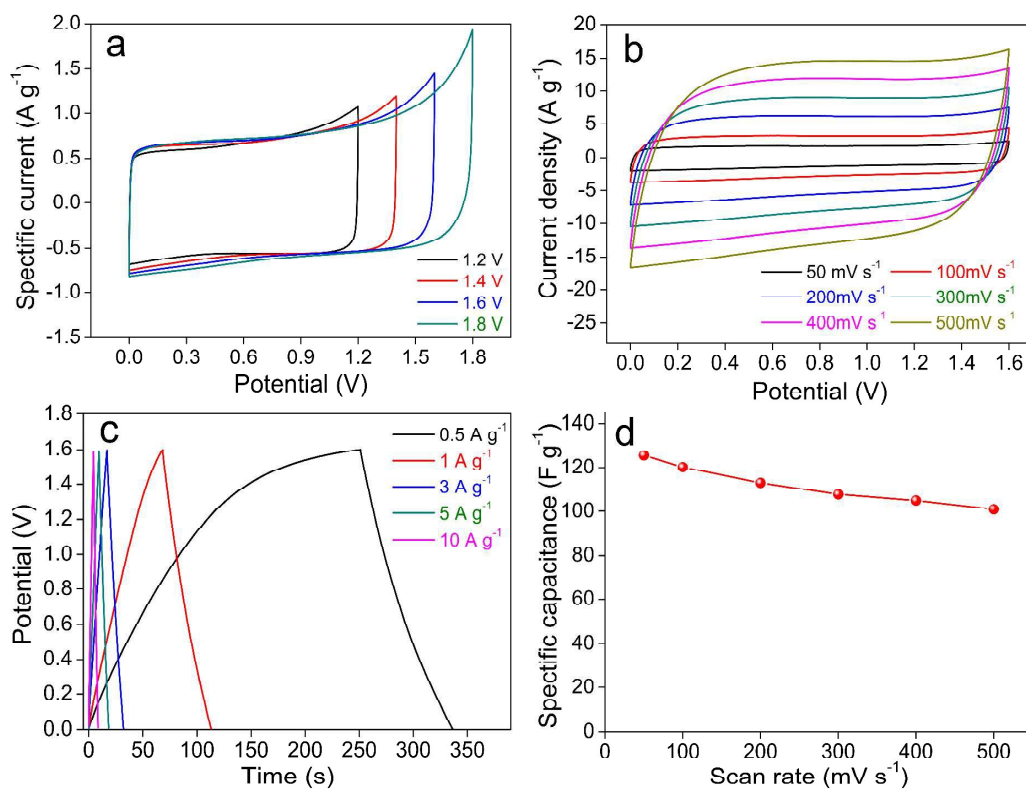(The inset is the comparison of GCD curves of the 1st and the 5000th cycle).

Fig.6 Electrochemical behaviors of AACS-6 measured in a two-electrode system in 0.5 M Na_2SO_4 aqueous electrolyte. (a) CV measurements at 20 mV s^{-1} in different voltage windows. (b) CV measurements at different scan rates in the potential range from 0 V to 1.6 V. (c) Galvanostatic charge-discharge profiles at different currents. (d) Specific capacitance of measured at different scan rates.
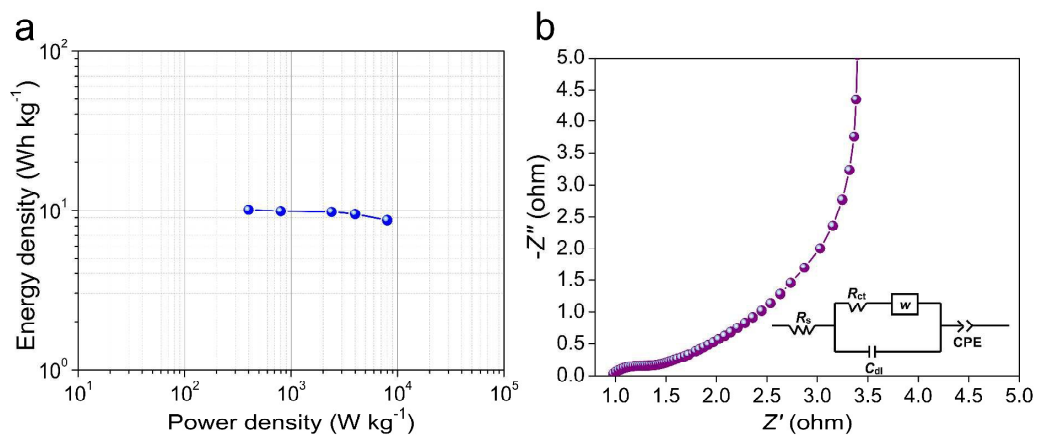
Fig. 7 Ragone plot (a) and Nyquist plot (b) of the symmetric supercapacitor in 0.5 M Na_2SO_4 aqueous

electrolyte.

Porous carbon spheres from resorcinol-formaldehyde resin are obtained by an air-assisted activation strategy, which shows excellent pore structures and superior electrochemical performance.